

Higher-order topological semimetal induced by altermagnet

Dengfeng Wang(王登风), Xiang Ji(吉祥), and Sen Cui(崔森)
Citation: Chin. Phys. B, 2026, 35 (**7**): 077510. DOI: 10.1088/1674-1056/ae6b35
http://cpb.iphy.ac.cn; http://iopscience.iop.org/cpb

What follows is a list of articles you may be interested in

First-principles investigation of magnetic properties in hyperkagome Mn_3TSi (T = Co, Rh, Ir) lattice

Peng Ren(任鹏), Xiaosheng Ni(倪晓升), Xunwu Hu(胡训武), and Kun Cao(曹坤)
Chin. Phys. B, 2026, 35 (**5**): 057502. DOI: 10.1088/1674-1056/ae156c

Recent progress on electron- and magnon-mediated torques

Jia-Min Lai(来嘉敏), Bingyue Bian(边冰玥), Zhonghai Yu(于忠海), Kaiwei Guo(郭凯卫), Yajing Zhang(张雅静), Pengnan Zhao(赵鹏楠), Xiaoqian Zhang(张霄倩), Chunyang Tang(汤春阳), Jiasen Cao(曹家森), Zhiyong Quan(全志勇), Fei Wang(王飞), and Xiaohong Xu(许小红)
Chin. Phys. B, 2025, 34 (**10**): 107501. DOI: 10.1088/1674-1056/add909

Effect of interlayer interaction on magnon properties of vdW honeycomb heterostructures

Jun Shan(单俊), Lichuan Zhang(张礼川), Huasu Fu(付华宿), Yuee Xie(谢月娥), Yuriy Mokrousov, and Yuanping Chen(陈元平)
Chin. Phys. B, 2025, 34 (**8**): 087501. DOI: 10.1088/1674-1056/adce97

Alternating spin splitting of electronic and magnon bands in two-dimensional altermagnetic materials

Qian Wang(王乾), Da-Wei Wu(邬大为), Guang-Hua Guo(郭光华), Meng-Qiu Long(龙孟秋), and Yun-Peng Wang(王云鹏)
Chin. Phys. B, 2024, 33 (**9**): 097507. DOI: 10.1088/1674-1056/ad6425

Evolution of anomalous Hall effect in ferromagnetic Weyl semimetal $Nb_xZr_{1-x}Co_2Sn$

Bo-Wen Chen(陈博文) and Bing Shen(沈冰)
Chin. Phys. B, 2024, 33 (**8**): 087501. DOI: 10.1088/1674-1056/ad4a3b

---

Higher-order topological semimetal induced by altermagnet

Dengfeng Wang(王登风), Xiang Ji(吉祥), and Sen Cui(崔森)†

Department of Physics, Jiangsu University, Zhenjiang 212013, *China*

(Received 11 March 2026; revised manuscript received 7 May 2026; accepted manuscript online 11 May 2026)

Altermagnetism, characterized by momentum-dependent spin splitting in the absence of net magnetization, provides a fertile ground for realizing topological states. Here, we show that coupling a first-order topological insulator to a *d*-wave altermagnet leads to a higher-order topological semimetal phase. This phase simultaneously hosts gap-closing points, robust zero-energy edge states, and corner states. The altermagnetic order parameter governs the motion of the gap-closing points within the Brillouin zone, while the Néel vector determines the spatial localization of the corner states. By mapping out the phase diagram, we identify topological transitions between trivial, higher-order insulating, and higher-order topological semimetal phases. Our findings establish altermagnetic heterostructures as a tunable platform for engineering higher-order topological phases in two dimensions.

Keywords: altermagnet, topological semimetal, high-order topological phase

PACS: 75.10.–b, 73.20.–r, 03.65.Vf

DOI: 10.1088/1674-1056/ae6b35 **CSTR:** 32038.14.CPB.ae6b35

1. Introduction

Altermagnetism has recently emerged as a distinct form of magnetism, characterized by compensating collinear spin structures connected by crystal rotational symmetries.[1] Combining key features of ferromagnets and antiferromagnets, altermagnets exhibit momentum-dependent spin splitting while maintaining symmetry-enforced zero net magnetization.[1–8] Considerable theoretical and experimental efforts have been devoted to uncovering altermagnetic materials such as RuO_2,[9–12] MnTe,[13–15] CrSb,[16–18] Mn_5Si_3,[19–21] and KV_2Se_2O.[22] Depending on crystal symmetry, altermagnets host distinct types of spin splitting, such as *d*-wave, *g*-wave, and *i*-wave, which provide fertile ground for physical phenomena,[23–32] including the anomalous Hall effect,[19,33–35] finite-momentum pairing,[36–38] higher-order insulators/superconductors,[39–43] and enhanced *d*-wave superconductivity,[44,45] with broad prospects for spintronics applications.

In recent decades, higher-order topological semimetals (HOTSMs) and higher-order topological insulators (HOTIs) have enriched the classification of topological materials.[46–67] In contrast to first-order topological phases, higher-order topological phases give rise to lower-dimensional topological states,[68–73] such as one-dimensional hinge states[74–76] or zero-dimensional corner states.[77–80] Topological semimetals, including Dirac and Weyl semimetals, are characterized by symmetry-protected band crossings that exhibit linear dispersion in the vicinity of isolated Dirac or Weyl points.[81–93] While prior works have predicted that heterostructures composed of a topological insulator and an altermagnet can realize higher-order insulators/superconductors,[40–42] the possibility of realizing HOTSMs in altermagnetic systems remains largely unexplored.

In this work, we demonstrate the realization of a HOTSM phase by coupling a first-order topological insulator to a *d*-wave altermagnet through the magnetic proximity effect. The resulting system simultaneously hosts gap-closing points in the bulk, zero-energy edge states spanning all four edges, and higher-order corner states. The corner states are localized at opposite corners of the square lattice and can be manipulated by the Néel vector. While Ref. [41] has demonstrated HOTI phases in altermagnet-coupled systems, our work extends this by revealing that in the strong altermagnetism regime, a HOTSM phase emerges, characterized by tunable bulk gap-closing points and analytically determined phase boundaries. The gap-closing points move within the Brillouin zone as the altermagnetic order parameter varies. By mapping the topological phase diagram, we identify phase transitions between trivial, HOTI, and HOTSM phases and reveal the interplay between altermagnetism and topological states. These findings establish a tunable mechanism for realizing HOTSM phases with altermagnets, providing a versatile platform for exploring higher-order topology in magnetic systems.

2. The Hamiltonian of the altermagnet model

We start with a first-order topological insulator in proximity to an altermagnet with *d*-wave spin splitting.[22] The Bloch Hamiltonian of this system takes the form

$$H(\boldsymbol{k}) = H_0(\boldsymbol{k}) + H_{\mathrm{AM}}(\boldsymbol{k}). \tag{1}$$

†Corresponding author. E-mail: scui@ujs.edu.cn

© 2026 Chinese Physical Society and IOP Publishing Ltd. All rights, including for text and data mining, AI training, and similar technologies, are reserved.

Here, $H_0(\boldsymbol{k}) = M(\boldsymbol{k})\sigma_z + \lambda \sin k_x s_y \sigma_x - \lambda \sin k_y s_x \sigma_x$ is a Bernevig–Hughes–Zhang (BHZ) model[94–98] with $M(\boldsymbol{k}) = m - t\cos k_x - t\cos k_y$. λ denotes the strength of spin-orbit coupling. $\sigma_{x,y,z}$ and $s_{x,y,z}$ are the Pauli matrices acting on the orbital and spin degrees of freedom, respectively. $H_{\mathrm{AM}}(\boldsymbol{k}) = 2J_{\mathrm{A}}(\cos k_x - \cos k_y)\ \boldsymbol{s}\cdot\hat{\boldsymbol{n}}$ describes the altermagnet with d-wave spin splitting, where $\hat{\boldsymbol{n}} = (\cos\phi,\ \sin\phi,\ 0)$ represents the direction of the Néel vector, and J_{A} denotes the altermagnetic order parameter. Here we select the Néel vector with $\phi = 3\pi/4$. The Hamiltonian preserves space-inversion symmetry ($\mathscr{P}$), given by $U_{\mathscr{P}}H(\boldsymbol{k})U_{\mathscr{P}}^{-1} = H(-\boldsymbol{k})$, where $U_{\mathscr{P}} = s_0\sigma_z$. Another relevant symmetry is chiral symmetry ($\mathscr{C}$), defined by $U_{\mathscr{C}}H(\boldsymbol{k})U_{\mathscr{C}}^{-1} = -H(\boldsymbol{k})$, where $U_{\mathscr{C}} = s_z\sigma_x$. Furthermore, along the high-symmetry line $k_x = -k_y$, the Hamiltonian retains mirror symmetry with $\mathscr{M} = i\sqrt{2}/2(s_x + s_y)$. The introduction of the altermagnetic term breaks time-reversal symmetry, providing a tunable mechanism to realize topological corner states.[41]

3. Topological corner modes and edge modes

To elucidate the emergence of the HOTSM phase, we examine the energy spectrum of the heterostructure under open boundary conditions (OBC) with $J_{\mathrm{A}} = 0.7$. Figure 1(a) displays the logarithm of the absolute values of the OBC eigenenergies, revealing that the gapless states marked in blue are nondegenerate. As shown in the inset of Fig. 1(a), the energy spectrum is gapless, confirming that the system is in a semimetallic phase. The corresponding probability distributions show that these states are localized along the boundaries of the square lattice (Figs. 1(b) and 1(c)), identifying them as topological edge states. In contrast, two degenerate eigenenergies marked in red exhibit probability distributions localized at the corners of the lattice, as shown in Fig. 1(d), indicating the presence of topological corner states.

To further characterize the localization properties of these eigenstates, we calculate the inverse participation ratio (IPR) of the eigenstates ψ_n, defined as

$$\mathrm{IPR} = \frac{\sum_i |\psi_{n,i}|^4}{\left(\sum_i |\psi_{n,i}|^2\right)^2}, \tag{2}$$

where i indexes the lattice sites. The IPR serves as a measure of spatial localization, distinguishing between extended and localized states. In the thermodynamic limit, $\lim_{L\to\infty}\mathrm{IPR} \to 0$ for extended states, while it remains finite for localized states in a finite lattice of linear size L ($L_x = L_y = L$). As shown in Fig. 1(e), the IPR of the edge states increases as their eigenenergies approach zero and reaches its maximum for the two degenerate corner states.

The inset of Fig. 1(e) shows the finite-size scaling of the IPR for both the edge state E_1 and the corner states $C_{1,2}$. The IPR of the edge state scales as $1/L$ and vanishes in the thermodynamic limit, confirming its extended nature along the edges. In contrast, the IPR of the corner states remains finite as $L \to \infty$, demonstrating their strong spatial localization. These scaling behaviors provide clear evidence for the coexistence of topological edge and corner states in the HOTSM phase.

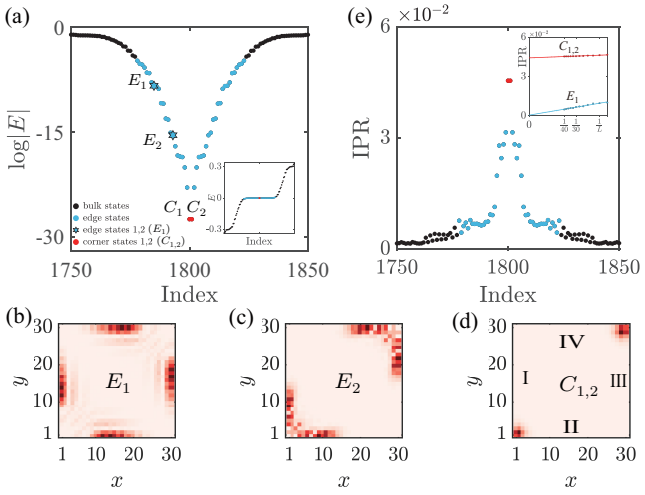


Fig. 1. (a) Energy spectrum ($\log|E|$) of a 30×30 square lattice under OBC, showing corner states (red), edge states (blue), and bulk states (black). The inset shows the energy spectrum. (b)–(d) Probability distributions of the edge states E_1, E_2, and corner states $C_{1,2}$, respectively. The four edges are labeled I, II, III, and IV in (d), which are used in the edge theory. (e) IPRs for corner states, edge states, and bulk states. The inset shows the finite-size scaling of the IPR for both the edge state E_1 and the corner states $C_{1,2}$. Other parameters are $J_{\mathrm{A}} = 0.7$, $m = 1.5$, and $\lambda = t = 1$.

4. Gap-closing points

In our two-dimensional (2D) system, the gapless nature of the bulk energy spectrum is accompanied by the emergence of higher-order corner states and edge states. The existence and spatial localization of these states are further corroborated by the probability distributions and numerical IPR analysis. To investigate the bulk gap-closing points, we compute the band structure under periodic boundary conditions (PBC) in both x and y directions, as shown in Fig. 2(a). The conduction and valence bands touch at nodes (cyan points), corresponding to gap-closing points. The positions of the gap-closing points within the Brillouin zone are shown in Fig. 2(b). The system has two pairs of gap-closing points, located in the regions of $(k_x > 0, k_y > 0)$ and $(k_x < 0, k_y < 0)$.

Under OBC in the x direction and PBC in the y direction (OBC_x–PBC_y), the energy spectrum reveals edge-localized states connecting the projections of the gap-closing points along this direction. We observe that zero-energy edge states appear as two segments, represented by the red curves in Fig. 2(c). To elucidate the spatial character of these segments, we present the probability distributions of the states with $E = 0$ at $k_y = 0$ and $k_y = \pi$, shown in Figs. 2(d1) and 2(d2), respectively. The probability distributions of the zero-energy states

(red points) confirm that these states are localized at the edges, while the corner states remain localized at the lattice corners. The coexistence of edge states, corner states, and bulk gap-closing points demonstrates that the newly emerged phase induced by strong altermagnetism corresponds to a 2D HOTSM phase.

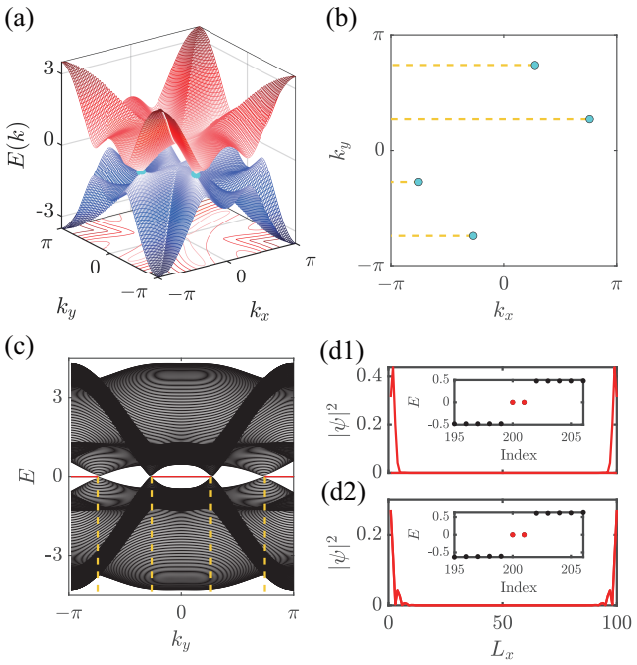


Fig. 2. (a) Band structure of the 2D HOTSM phase under PBC, with cyan points indicating gap-closing points. (b) Positions of the gap-closing points (cyan points) in the Brillouin zone. (c) Energy spectrum under OBC$_x$–PBC$_y$. Red lines denote zero-energy edge states. (d1), (d2) Probability distributions and energy spectra corresponding to the zero-energy edge states at $k_y = 0$ and $k_y = \pi$, respectively. Parameters are $J_A = 0.7$, $m = 1.5$, and $\lambda = t = 1$.

5. Topological phase diagram

The system exhibits different topological phases as the altermagnetic order parameter J_A is varied. In the absence of altermagnetism, the energy spectrum under OBC$_x$–PBC$_y$, shown in Fig. 3(a), exhibits gapless edge states. Upon increasing the altermagnetism to $J_A = 0.2$, a gap opens in the edge states, as shown in Fig. 3(b). Further increasing the altermagnetism to $J_A = 0.375$ leads to a band crossing at $k_y = 0$ and $k_y = \pm\pi$, as depicted in Fig. 3(c). The band crossing indicates a phase transition from an insulator to a semimetal.

Interestingly, the altermagnet also affects the positions of the gap-closing points in the Brillouin zone. Figure 3(d) shows their positions in the Brillouin zone for $J_A = 0.375$ and $J_A = 0.7$. For $J_A = 0.375$, the gap-closing points are located at $(0,\ \pi)$, $(0,\ -\pi)$, $(-\pi,\ 0)$, and $(\pi,\ 0)$, and are highlighted by blue pentagrams. For strong altermagnetism with $J_A = 0.7$, the gap-closing points are marked by cyan points. As J_A increases from 0.375 to 0.7, the gap-closing points move from the blue pentagrams to the cyan points, as indicated by the arrow in Fig. 3(d). This demonstrates that the locations of the gap-closing points are tunable via the altermagnetic order parameter J_A.

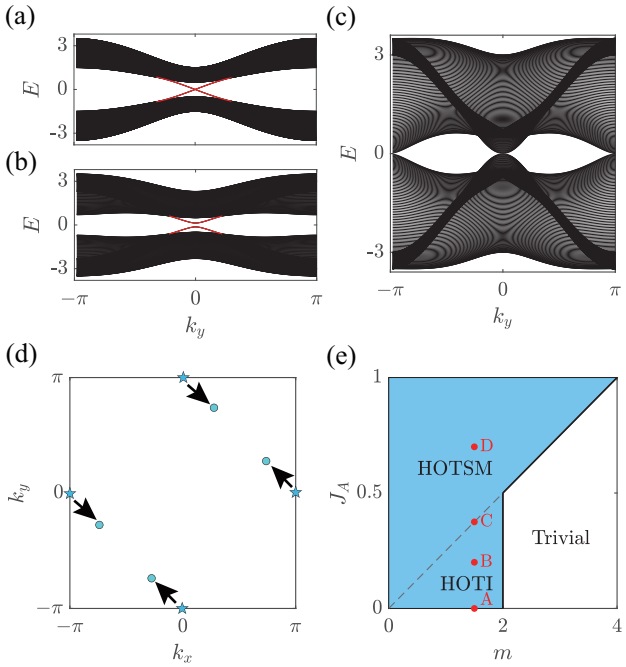


Fig. 3. (a) and (b) Energy spectra under OBC$_x$–PBC$_y$ for $J_A = 0$ and $J_A = 0.2$, respectively. Red-highlighted lines denote edge states. (c) Energy spectrum at $J_A = 0.375$ with the same boundary conditions, showing the band crossing at $k_y = 0$ and $k_y = \pm\pi$. (d) Positions of the gap-closing points in the Brillouin zone at $J_A = 0.375$ (blue pentagrams) and $J_A = 0.7$ (cyan points). Arrows indicate the motion of the gap-closing points with increasing J_A. (e) Phase diagram in J_A–m space: blue and white regions represent the topological phase and trivial phase, respectively. Solid lines mark topological phase boundaries, and dashed lines separate HOTSM and HOTI phases. Points A (1.5, 0), B (1.5, 0.2), C (1.5, 0.375), and D (1.5, 0.7) correspond to the parameters used in panels (a)–(c) and Fig. 2(c), respectively.

To clearly understand and determine the phase boundaries, we calculate the gap-closing conditions. The analytical energy spectrum of the system, obtained from the Hamiltonian in Eq. (1), is given by

$$\varepsilon_k = \pm\sqrt{\pm\sqrt{(2M(\boldsymbol{k})J(\boldsymbol{k}))^2 + \lambda_J^2} + M(\boldsymbol{k})^2 + J(\boldsymbol{k})^2 + \lambda_{xy}^2}, \quad (3)$$

where $J(\boldsymbol{k}) = 2J_A(\cos k_x - \cos k_y)$, $\lambda_J = 2J(\boldsymbol{k})\lambda \sin k_x \sin\phi - 2J(\boldsymbol{k})\lambda \sin k_y \cos\phi$, and $\lambda_{xy}^2 = (\lambda \sin k_x)^2 + (\lambda \sin k_y)^2$. We choose the Néel vector with $\phi = (2n+1)\pi/4$, $n \in \mathbb{Z}$. Let $\varepsilon_k = 0$, then $\sin k_{x/y} = 0$ and $\cos k_{x/y} = \pm 1$. Therefore, the gap-closing conditions are as follows:

$$J_A^c = \pm\frac{1}{4}m,\ m = \pm 2t. \quad (4)$$

The realization of the HOTSM phase relies on the d-wave symmetry of altermagnetism, characterized by the momentum-dependent form $2J_A(\cos k_x - \cos k_y)$. This governs the emergence and motion of the gap-closing points, leading to the analytical phase boundary $J_A^c = \pm m/4$ that delineates the transition between the HOTSM and HOTI phases. According to Eq. (4), we choose the altermagnetic parameter J_A and the mass parameter m as tuning parameters, and the phase diagram

of the system is shown in Fig. 3(e). The blue region in the diagram represents the topological phase, the white region represents the trivial phase, and the dashed lines represent the phase boundaries between the HOTSM and HOTI phases. When $J_{\rm A}^{\rm c} < J_{\rm A} < 1$ and $0 < m < 4$, the bulk band structure is gapless. The system hosts two pairs of gap-closing points accompanied by higher-order topological states, corresponding to the HOTSM phase. The HOTSM phase extends into the region $m > 2$, where the first-order topological insulator becomes trivial. This demonstrates that the higher-order topology in our system originates intrinsically from altermagnetism-induced Jackiw–Rebbi mass domain walls at the corners, which will be discussed in Section 6. When $0 < J_{\rm A} < J_{\rm A}^{\rm c}$ and $0 < m < 2$, the bulk bands are gapped and the edge states are also gapped, indicating that the system is in the HOTI phase. When $J_{\rm A} = 0$ and $0 < m < 2$, the bulk bands remain gapped, but the edge states become gapless, and the system is in the first-order topological insulator phase. These analytical results are fully consistent with our numerical calculations. The specific parameter points labeled A, B, C, and D in the phase diagram correspond to the physical properties shown in Figs. 2(c) and 3(a)–3(c), respectively.

6. Edge theory

To elucidate the emergence of corner states, we analyze the system using edge theory in the low-energy limit. Expanding the Hamiltonian to second order in momentum around $\boldsymbol{k} = (0,\ \pi)$, the resulting low-energy Hamiltonian takes the form

$$\begin{aligned} H(\boldsymbol{k}) \ =\ & m\sigma_z + 4J_{\rm A}\ \boldsymbol{s}\cdot\hat{\boldsymbol{n}} + \frac{t}{2}(k_x^2 - k_y^2)\sigma_z + \lambda k_x s_y \sigma_x \\ & + \lambda k_y s_x \sigma_x - J_{\rm A}(k_x^2 + k_y^2)\boldsymbol{s}\cdot\hat{\boldsymbol{n}}. \end{aligned} \tag{5}$$

For clarity, we label the four edges of the square lattice as I, II, III, and IV, as illustrated in Fig. 1(d). For edge I, we substitute k_x with $-\mathrm{i}\partial_x$ and neglect the higher-order k_y^2 term. $H(\boldsymbol{k})$ can be decomposed as $H = H_0 + H_{\rm p}$, where

$$H_0(-\mathrm{i}\partial_x, k_y) = m\sigma_z + 4J_{\rm A}\ \boldsymbol{s}\cdot\hat{\boldsymbol{n}} - \frac{t}{2}\partial_x^2\sigma_z - \mathrm{i}\lambda\partial_x s_y\sigma_x, \tag{6}$$

$$H_{\rm p}(-\mathrm{i}\partial_x, k_y) = \lambda k_y s_x\sigma_x + J_{\rm A}\partial_x^2(s_x\cos\phi + s_y\sin\phi). \tag{7}$$

Projecting H_0 onto the eigenstates of $\boldsymbol{s}\cdot\hat{\boldsymbol{n}}$, which satisfy $\boldsymbol{s}\cdot\hat{\boldsymbol{n}}\,|\chi_\pm\rangle = \pm|\chi_\pm\rangle$, decomposes the system into two decoupled spin sectors. Within each sector, the effective Hamiltonian reads $H_0^{\rm eff}(-\mathrm{i}\partial_x, k_y) = m'\sigma_z - \frac{t}{2}\partial_x^2\sigma_z - \mathrm{i}\lambda\partial_x s_y\sigma_x$ with $m' = m \pm 4J_{\rm A}$.

By solving the eigenvalue equation $H_0^{\rm eff}\psi_\alpha(x) = E_\alpha\psi_\alpha(x)$ under the boundary conditions $\psi_\alpha(0) = \psi_\alpha(+\infty) = 0$ with $E_\alpha = 0$, we obtain two corresponding Jackiw–Rebbi solutions

$$\psi_\alpha(x) = \phi(x)\xi_\alpha = \mathcal{N}_x\sin(\kappa_1 x)\,\mathrm{e}^{\kappa_2 x}\,\mathrm{e}^{\mathrm{i}k_y y}\xi_\alpha, \tag{8}$$

with $\kappa_1 = \sqrt{-2m'/t - \lambda^2/t^2}$ and $\kappa_2 = -\lambda/t$. The normalization factor is $\mathcal{N}_x = \sqrt{-4\kappa_2(\kappa_1^2 + \kappa_2^2)/\kappa_1^2}$. The normalization of the wave function requires $\kappa_1^2 + \kappa_2^2 > 0$, which implies $m' < 0$.

The eigenvectors ξ_α satisfy $s_y\sigma_y\xi_\alpha = \xi_\alpha$. A convenient explicit choice is

$$\begin{aligned} \xi_1 \ &=\ |s_y = +1\rangle \otimes |\sigma_y = +1\rangle, \\ \xi_2 \ &=\ |s_y = -1\rangle \otimes |\sigma_y = -1\rangle. \end{aligned} \tag{9}$$

Thus, the effective Hamiltonian for edge I is $H_{{\rm I},\alpha\beta}(k_y) = \int_0^{+\infty}\mathrm{d}x\psi_\alpha^*(x)H_{\rm p}(-\mathrm{i}\partial_x, k_y)\psi_\beta(x)$. Similarly, for the other edges, the effective edge Hamiltonians can be written as

$$\begin{aligned} H_{\rm I}(k_y) &= -\lambda k_y s_x - (2m'/t)J_{\rm A}\sin\phi s_z, \\ H_{\rm II}(k_x) &= +\lambda k_x s_x - (2m'/t)J_{\rm A}\cos\phi s_z, \\ H_{\rm III}(k_y) &= +\lambda k_y s_x + (2m'/t)J_{\rm A}\sin\phi s_z, \\ H_{\rm IV}(k_x) &= -\lambda k_x s_x + (2m'/t)J_{\rm A}\cos\phi s_z. \end{aligned} \tag{10}$$

We define an edge coordinate l in the anticlockwise direction. The effective edge Hamiltonian can be expressed as

$$H_{\rm edge} = -\mathrm{i}A(l)s_x\partial_l + M(l)s_z, \tag{11}$$

with $A(l) = \lambda$ and the mass term $M(l) = -(2m'/t)J_{\rm A}\sin\phi$, $-(2m'/t)J_{\rm A}\cos\phi$, $(2m'/t)J_{\rm A}\sin\phi$, and $(2m'/t)J_{\rm A}\cos\phi$ for edges I, II, III, and IV, respectively.

Based on the edge theory analysis, the spatial localization of the corner states is primarily governed by the in-plane orientation of the Néel vector. Notably, the HOTSM phase extends into the region $m > 2$, where the first-order topological insulator becomes trivial. The higher-order topology in our system originates from altermagnet-induced mass domain walls at the corners. Specifically, when $\phi \bmod 2\pi \in (0, \pi/2) \cup (\pi, 3\pi/2)$, the mass terms change sign between edges I and IV, as well as between edges II and III, giving rise to mass domain walls at the left-up and right-down corners, where corner states emerge. In contrast, for $\phi \bmod 2\pi \in (\pi/2, \pi) \cup (3\pi/2, 2\pi)$, the sign reversal of mass terms occurs between edges I and II, and between edges III and IV, resulting in corner modes localized at the left-down and right-up corners. The mass terms vanish on edges II and IV for $\phi = \pi/2$, and on edges I and III for $\phi = \pi$, thereby suppressing the formation of corner states. These results demonstrate that the spatial positions of the corner states can be tuned by controlling the Néel vector.

7. The influence of the Néel vector on the topological states

To confirm the absence of corner states for the Néel vector oriented along $\phi = n\pi/2$ ($n \in \mathbb{Z}$), we show the energy spectrum under OBC for $\phi = \pi/2$ in Fig. 4(a). The system

hosts only edge states whose energies are marked in blue. The original higher-order corner states transform into edge states, whose energies are represented by blue diamonds. The probability distributions of these edge states are localized at the upper and lower edges of the lattice, as shown in the inset of Fig. 4(a). The band structure under PBC, shown in Fig. 4(b), reveals that the Néel vector also governs the positions of the gap-closing points. For $\phi = \pi/2$, the two pairs of gap-closing points are located along the $k_y = 0$ and $k_y = \pi$ lines. Under OBC$_x$–PBC$_y$, the energy spectrum lacks zero-energy edge states, as shown in Fig. 4(c). In contrast, under PBC$_x$–OBC$_y$, as illustrated in Fig. 4(d), zero-energy edge states appear in the energy spectrum. This confirms that the system retains its fundamental topological semimetal character despite the disappearance of the higher-order corner states.

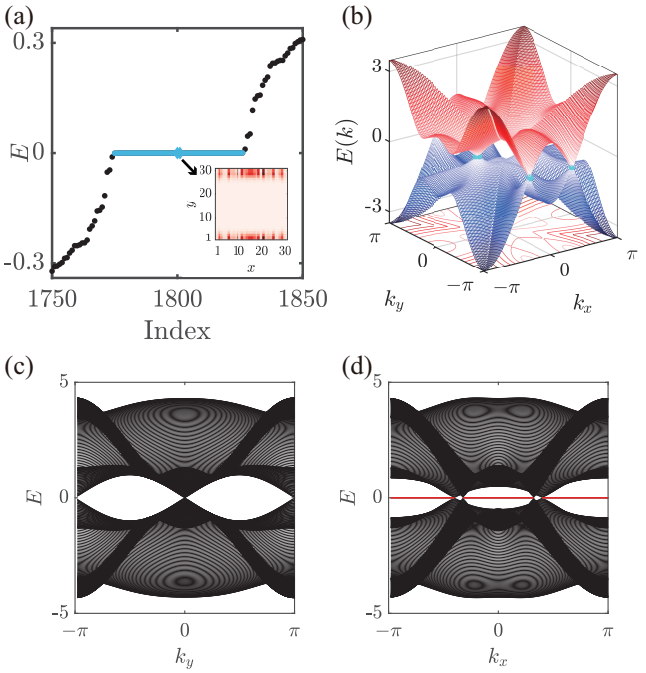


Fig. 4. (a) Energy spectrum without higher-order corner states. Blue and black points denote the energies of edge states and bulk states, respectively. The inset shows the probability distributions of states whose energies are highlighted by diamonds. (b) Band structure of the conventional topological semimetal phase, with cyan points indicating gap-closing points. (c) Energy spectrum under OBC$_x$–PBC$_y$, showing the absence of zero-energy edge states. (d) Energy spectrum under PBC$_x$–OBC$_y$, with red-highlighted lines indicating zero-energy edge states. Parameters are $J_A = 0.7$, $m = 1.5$, and $\phi = \pi/2$.

8. Conclusion

In summary, we have demonstrated that altermagnetism can induce a topological insulator into a HOTSM phase. The system simultaneously hosts corner states, one-dimensional (1D) edge states, and bulk gap-closing points whose positions shift within the Brillouin zone as the altermagnetic order parameter J_A is varied. A tunable phase diagram governed by the altermagnetic order parameter and mass parameter is established, revealing clearly defined phase boundaries between trivial, HOTI, and HOTSM phases. Furthermore, we have elucidated the crucial role of the Néel vector direction in governing the system's topological properties: it controls the emergence of corner states, determines the positions of gap-closing points, and regulates the emergence of zero-energy edge states through boundary conditions.

Recent experiments have demonstrated that KV_2Se_2O is a metallic room-temperature altermagnet with d-wave spin-momentum locking.[22] This provides a candidate material for implementing our proposal. The resulting topological corner states could be detected using scanning tunneling microscopy (STM). For the Néel vector, relevant studies have been conducted in antiferromagnetic materials to manipulate and detect it through current, strain, voltage, or spin-orbit torque.[99–104] Similar methods can also be used to manipulate the Néel vector in altermagnets. This work is expected to promote further investigations of higher-order topological phenomena in altermagnets.

Acknowledgment

We are grateful for the enlightening discussions with Prof. Zhenling Wang.

References

[1] Šmejkal L, Sinova J and Jungwirth T 2022 *Phys. Rev. X* **12** 040501
[2] Šmejkal L, Sinova J and Jungwirth T 2022 *Phys. Rev. X* **12** 031042
[3] Bai L, Feng W, Liu S, Šmejkal L, Mokrousov Y and Yao Y 2024 *Adv. Funct. Mater.* **34** 2409327
[4] Jiang Y, Song Z, Zhu T, Fang Z, Weng H, Liu Z X, Yang J and Fang C 2024 *Phys. Rev. X* **14** 031039
[5] McClarty P A and Rau J G 2024 *Phys. Rev. Lett.* **132** 176702
[6] Rimmler B H, Pal B and Parkin S S P 2024 *Nat. Rev. Mater.* **10** 109
[7] Song C, Bai H, Zhou Z, Han L, Reichlova H, Dil J H, Liu J, Chen X and Pan F 2025 *Nat. Rev. Mater.* **10** 473
[8] Zhang F, Cheng X, Yin Z, Liu C, Deng L, Qiao Y, Shi Z, Zhang S, Lin J, Liu Z, Ye M, Huang Y, Meng X, Zhang C, Okuda T, Shimada K, Cui S, Zhao Y, Cao G H, Qiao S, Liu J and Chen C 2025 *Nat. Phys.* **21** 760
[9] Zhu Z H, Strempfer J, Rao R R, Occhialini C A, Pelliciari J, Choi Y, Kawaguchi T, You H, Mitchell J F, Shao-Horn Y and Comin R 2019 *Phys. Rev. Lett.* **122** 017202
[10] Šmejkal L, González-Hernández R, Jungwirth T and Sinova J 2020 *Sci. Adv.* **6** eaaz8809
[11] Bai H, Han L, Feng X Y, Zhou Y J, Su R X, Wang Q, Liao L Y, Zhu W X, Chen X Z, Pan F, Fan X L and Song C 2022 *Phys. Rev. Lett.* **128** 197202
[12] Fedchenko O, Minár J, Akashdeep A, D'Souza S W, Vasilyev D, Tkach O, Odenbreit L, Nguyen Q, Kutnyakhov D, Wind N, Wenthaus L, Scholz M, Rossnagel K, Hoesch M, Aeschlimann M, Stadtmüller B, Kläui M, Schönhense G, Jungwirth T, Hellenes A B, Jakob G, Šmejkal L, Sinova J and Elmers H J 2024 *Sci. Adv.* **10** eadj4883
[13] Amin O J, Dal Din A, Golias E, Niu Y, Zakharov A, Fromage S C, Fields C J B, Heywood S L, Cousins R B, Maccherozzi F, Krempaský J, Dil J H, Kriegner D, Kiraly B, Campion R P, Rushforth A W, Edmonds K W, Dhesi S S, Šmejkal L, Jungwirth T and Wadley P 2024 *Nature* **636** 348
[14] Gonzalez Betancourt R D, Zubáč J, Geishendorf K, Ritzinger P, Růžičková B, Kotte T, Železný J, Olejník K, Springholz G, Büchner B, Thomas A, Výborný K, Jungwirth T, Reichlová H and Kriegner D 2024 *npj Spintronics* **2** 45
[15] Lee S, Lee S, Jung S, Jung J, Kim D, Lee Y, Seok B, Kim J, Park B G, Šmejkal L, Kang C J and Kim C 2024 *Phys. Rev. Lett.* **132** 036702

[16] Reimers S, Odenbreit L, Šmejkal L, Strocov V N, Constantinou P, Hellenes A B, Jaeschke Ubiergo R, Campos W H, Bharadwaj V K, Chakraborty A, Denneulin T, Shi W, Dunin-Borkowski R E, Das S, Kläui M, Sinova J and Jourdan M 2024 *Nat. Commun.* **15** 2116
[17] Zhou Z, Cheng X, Hu M, Chu R, Bai H, Han L, Liu J, Pan F and Song C 2025 *Nature* **638** 645
[18] Yang G, Li Z, Yang S, Li J, Zheng H, Zhu W, Pan Z, Xu Y, Cao S, Zhao W, Jana A, Zhang J, Ye M, Song Y, Hu L H, Yang L, Fujii J, Vobornik I, Shi M, Yuan H, Zhang Y, Xu Y and Liu Y 2025 *Nat. Commun.* **16** 1442
[19] Reichlova H, Lopes Seeger R, González-Hernández R, Kounta I, Schlitz R, Kriegner D, Ritzinger P, Lammel M, Leiviskä M, Birk Hellenes A, Olejník K, Petříček V, Doležal P, Horak L, Schmoranzerova E, Badura A, Bertaina S, Thomas A, Baltz V, Michez L, Sinova J, Goennenwein S T B, Jungwirth T and Šmejkal L 2024 *Nat. Commun.* **15** 4961
[20] Leiviskä M, Rial J, Bad'ura A, Seeger R L, Kounta I, Beckert S, Kriegner D, Joumard I, Schmoranzerová E, Sinova J, Gomonay O, Thomas A, Goennenwein S T B, Reichlová H, Šmejkal L, Michez L, Jungwirth T and Baltz V 2024 *Phys. Rev. B* **109** 224430
[21] Badura A, Campos W H, Bharadwaj V K, Kounta I, Michez L, Petit M, Rial J, Leiviskä M, Baltz V, Krizek F, Kriegner D, Železný J, Zemen J, Telkamp S, Sailler S, Lammel M, Jaeschke-Ubiergo R, Hellenes A B, González-Hernández R, Sinova J, Jungwirth T, Goennenwein S T B, Šmejkal L and Reichlova H 2025 *Nat. Commun.* **16** 7111
[22] Jiang B, Hu M, Bai J, Song Z, Mu C, Qu G, Li W, Zhu W, Pi H, Wei Z, Sun Y J, Huang Y, Zheng X, Peng Y, He L, Li S, Luo J, Li Z, Chen G, Li H, Weng H and Qian T 2025 *Nat. Phys.* **21** 754
[23] Ouassou J A, Brataas A and Linder J 2023 *Phys. Rev. Lett.* **131** 076003
[24] Zhu D, Zhuang Z Y, Wu Z and Yan Z 2023 *Phys. Rev. B* **108** 184505
[25] Sun C, Brataas A and Linder J 2023 *Phys. Rev. B* **108** 054511
[26] Brekke B, Sukhachov P, Giil H G, Brataas A and Linder J 2024 *Phys. Rev. Lett.* **133** 236703
[27] Wang Q, Wu D W, Guo G H, Long M Q and Wang Y P 2024 *Chin. Phys. B* **33** 097507
[28] Antonenko D S, Fernandes R M and Venderbos J W F 2025 *Phys. Rev. Lett.* **134** 096703
[29] Lin H J, Zhang S B, Lu H Z and Xie X C 2025 *Phys. Rev. Lett.* **134** 136301
[30] Zhu Y, Liu S, Cui Q, Jiang J, Yang H, Zhou T and Liu B 2025 *Appl. Phys. Lett.* **127** 082401
[31] Li J, Li W, Hu Y, Guo X, Chen M, Li S, Chen X and Wu S 2025 *Appl. Phys. Lett.* **127** 132401
[32] González J W, Gallardo R A, Vidal-Silva N and León A M 2026 *Chin. Phys. Lett.* **43** 020705
[33] Feng Z, Zhou X, Šmejkal L, Wu L, Zhu Z, Guo H, González-Hernández R, Wang X, Yan H, Qin P, Zhang X, Wu H, Chen H, Meng Z, Liu L, Xia Z, Sinova J, Jungwirth T and Liu Z 2022 *Nat. Electron.* **5** 735
[34] Sato T, Haddad S, Fulga I C, Assaad F F and Van Den Brink J 2024 *Phys. Rev. Lett.* **133** 086503
[35] Chen R, Wang Z M, Wu K, Sun H P, Zhou B, Wang R and Xu D H 2025 *Phys. Rev. Lett.* **135** 096602
[36] Zhang S B, Hu L H and Neupert T 2024 *Nat. Commun.* **15** 1801
[37] Chakraborty D and Black-Schaffer A M 2024 *Phys. Rev. B* **110** L060508
[38] Chakraborty D and Black-Schaffer A M 2025 *Phys. Rev. B* **112** 014516
[39] Li Y X and Liu C C 2023 *Phys. Rev. B* **108** 205410
[40] Ghorashi S A A, Hughes T L and Cano J 2024 *Phys. Rev. Lett.* **133** 106601
[41] Li Y X, Liu Y and Liu C C 2024 *Phys. Rev. B* **109** L201109
[42] Li Y X 2024 *Phys. Rev. B* **109** 224502
[43] Guo X, Zhang M H and Yao D X 2025 *Chin. Phys. Lett.* **42** 120703
[44] Bose A, Vadnais S and Paramekanti A 2024 *Phys. Rev. B* **110** 205120
[45] Li J, Liu J, Yang X and Tang H K 2025 arXiv:2505.12342
[46] Schnyder A P, Ryu S, Furusaki A and Ludwig A W W 2008 *Phys. Rev. B* **78** 195125
[47] Hasan M Z and Kane C L 2010 *Rev. Mod. Phys.* **82** 3045
[48] Mesaros A and Ran Y 2013 *Phys. Rev. B* **87** 155115
[49] Chiu C K, Teo J C Y, Schnyder A P and Ryu S 2016 *Rev. Mod. Phys.* **88** 035005
[50] Bansil A, Lin H and Das T 2016 *Rev. Mod. Phys.* **88** 021004
[51] Kudo K, Yoshida T and Hatsugai Y 2019 *Phys. Rev. Lett.* **123** 196402
[52] Ghorashi S A A, Li T and Hughes T L 2020 *Phys. Rev. Lett.* **125** 266804
[53] Ghorashi S A A, Hughes T L and Rossi E 2020 *Phys. Rev. Lett.* **125** 037001
[54] Wang H X, Lin Z K, Jiang B, Guo G Y and Jiang J H 2020 *Phys. Rev. Lett.* **125** 146401
[55] Tiwari A, Li M H, Bernevig B A, Neupert T and Parameswaran S A 2020 *Phys. Rev. Lett.* **124** 046801
[56] Xi W, Zhang Z H, Gu Z C and Chen W Q 2021 *Sci. Bull.* **66** 1731
[57] Liu T, He J J, Yang Z and Nori F 2021 *Phys. Rev. Lett.* **127** 196801
[58] Cao Y, Li Y and Yang X 2021 *Phys. Rev. B* **103** 075126
[59] Proctor M, Blanco de Paz M, Bercioux D, García-Etxarri A and Arroyo Huidobro P 2021 *Appl. Phys. Lett.* **118** 091105
[60] Song L, Yang H, Cao Y and Yan P 2022 *Nat. Commun.* **13** 5601
[61] Li Y, Ji X, Chen Y, Yan X and Yang X 2022 *Phys. Rev. B* **106** 195425
[62] Zheng Z, Yin J, Wen J and Yu D 2022 *Appl. Phys. Lett.* **120** 144101
[63] Jahin A, Tiwari A and Wang Y 2022 *SciPost Phys.* **12** 053
[64] Xiong Z, Lin Z K, Wang H X, Liu S, Qian Y and Jiang J H 2023 *Phys. Rev. B* **108** 085141
[65] Guo S, Huang J, Huang R, Zhuang F, Su S, Lin Z, Qiu W, Su J and Wang X 2024 *Appl. Phys. Lett.* **124** 073104
[66] Ji X, Geng H, Akhtar N and Yang X 2025 *Phys. Rev. B* **111** 195419
[67] Liu L, Sun Q F and Zhang Y T 2025 arXiv:2502.13535
[68] Khalaf E 2018 *Phys. Rev. B* **97** 205136
[69] Yan Z 2019 *Phys. Rev. Lett.* **123** 177001
[70] Tiwari A, Jahin A and Wang Y 2020 *Phys. Rev. Res.* **2** 043300
[71] Xie B, Wang H X, Zhang X, Zhan P, Jiang J H, Lu M and Chen Y 2021 *Nat. Rev. Phys.* **3** 520
[72] Wang Z, Meng Y, Yan B, Zhao D, Yang L, Chen J, Cheng M, Xiao T, Shum P P, Liu G G, Yang Y, Chen H, Xi X, Zhu Z X, Xie B and Gao Z 2025 *Nat. Commun.* **16** 3122
[73] Yang X, Feng Y, Wahab A and Geng H 2026 *Phys. Rev. A* **113** 023506
[74] Benalcazar W A, Bernevig B A and Hughes T L 2017 *Phys. Rev. B* **96** 245115
[75] Yan Z 2019 *Phys. Rev. B* **100** 205406
[76] Zhao W, Yang M, Xu R, Du X, Li Y, Zhai K, Peng C, Pei D, Gao H, Li Y, Xu L, Han J, Huang Y, Liu Z, Yao Y, Zhuang J, Du Y, Zhou J, Chen Y and Yang L 2023 *Nat. Commun.* **14** 8089
[77] Luo X W and Zhang C 2019 *Phys. Rev. Lett.* **123** 073601
[78] Ren Y, Qiao Z and Niu Q 2020 *Phys. Rev. Lett.* **124** 166804
[79] Roy B and Juričić V 2021 *Phys. Rev. B* **104** L180503
[80] Ji X, Ding W, Chen Y and Yang X 2024 *Phys. Rev. B* **109** 125420
[81] Vazifeh M M and Franz M 2013 *Phys. Rev. Lett.* **111** 027201
[82] Soluyanov A A, Gresch D, Wang Z, Wu Q, Troyer M, Dai X and Bernevig B A 2015 *Nature* **527** 495
[83] Sun X Q, Zhang S C and Wang Z 2015 *Phys. Rev. Lett.* **115** 076802
[84] Yan Z and Wang Z 2016 *Phys. Rev. Lett.* **117** 087402
[85] Yan B and Felser C 2017 *Annu. Rev. Condens. Matter Phys.* **8** 337
[86] Yesilyurt C, Siu Z B, Tan S G, Liang G, Yang S A and Jalil M B A 2017 *Appl. Phys. Lett.* **111** 063101
[87] Armitage N P, Mele E J and Vishwanath A 2018 *Rev. Mod. Phys.* **90** 015001
[88] Geishendorf K, Schlitz R, Vir P, Shekhar C, Felser C, Nielsch K, Goennenwein S T B and Thomas A 2019 *Appl. Phys. Lett.* **114** 092403
[89] Shen J, Zeng Q, Zhang S, Tong W, Ling L, Xi C, Wang Z, Liu E, Wang W, Wu G and Shen B 2019 *Appl. Phys. Lett.* **115** 212403
[90] Da H, Song Q, Ye H and Yan X 2021 *Appl. Phys. Lett.* **119** 081103
[91] Tang K, Wen Z, Lau Y C, Sukegawa H, Seki T and Mitani S 2021 *Appl. Phys. Lett.* **118** 062402
[92] Bierhance G, Markou A, Gueckstock O, Rouzegar R, Behovits Y, Chekhov A L, Wolf M, Seifert T S, Felser C and Kampfrath T 2022 *Appl. Phys. Lett.* **120** 082401
[93] Matsuo T, Higo T, Nishio-Hamane D and Nakatsuji S 2022 *Appl. Phys. Lett.* **121** 013103
[94] Bernevig B A, Hughes T L and Zhang S C 2006 *Science* **314** 1757
[95] Qian X, Liu J, Fu L and Li J 2014 *Science* **346** 1344
[96] Yan Z, Song F and Wang Z 2018 *Phys. Rev. Lett.* **121** 096803
[97] Wu S, Fatemi V, Gibson Q D, Watanabe K, Taniguchi T, Cava R J and Jarillo-Herrero P 2018 *Science* **359** 76
[98] Li Y Y and Zhang S B 2025 *Phys. Rev. B* **111** 045106
[99] Godinho J, Reichlová H, Kriegner D, Novák V, Olejník K, Kašpar Z, Šobáň Z, Wadley P, Campion R P, Otxoa R M, Roy P E, Železný J, Jungwirth T and Wunderlich J 2018 *Nat. Commun.* **9** 4686
[100] Park I J, Lee T, Das P, Debnath B, Carman G P and Lake R K 2019 *Appl. Phys. Lett.* **114** 142403
[101] Mahmood A, Echtenkamp W, Street M, Wang J L, Cao S, Komesu T, Dowben P A, Buragohain P, Lu H, Gruverman A, Parthasarathy A, Rakheja S and Binek C 2021 *Nat. Commun.* **12** 1674
[102] Zhang P, Chou C T, Yun H, McGoldrick B C, Hou J T, Mkhoyan K A and Liu L 2022 *Phys. Rev. Lett.* **129** 017203
[103] Grigorev V, Filianina M, Lytvynenko Y, Sobolev S, Pokharel A R, Lanz A P, Sapozhnik A, Kleibert A, Bodnar S, Grigorev P, Skourski Y, Kläui M, Elmers H J, Jourdan M and Demsar J 2022 *ACS Nano* **16** 20589
[104] Guo H, Lin Z, Lu J, Yun C, Han G, Sun S, Wu Y, Yang W, Xiao D, Zhu Z, Peng L, Ye Y, Hou Y, Yang J and Luo Z 2025 *Nat. Commun.* **16** 8911